Macromolecular Research
https://doi.org/10.1007/s13233-025-00405-7

Online ISSN 2092-7673
Print ISSN 1598-5032

ARTICLE

Biomimetic chitosan-based scaffold for 3D breast cancer cell culture: a promising tool for anticancer drug screening

Agustina Setiawati[1] · Nyoman Bayu Wisnu Kencana[1] · Hendrik Satria Dwi Putra[1] · Maria Violita Sekar Ayu Kencana[1] · Olatunji Ajiteru[2] · I Made Bayu Kresna Yoga[3,4] · Nurul Fatimah[3,4] · Adam Hermawan[3,4]

Received: 14 November 2024 / Revised: 17 March 2025 / Accepted: 23 March 2025

Abstract

Natural biodegradable polymers have been extensively studied as scaffolds for three-dimensional (3D) cancer cell culture in high-throughput screening (HTS) for anticancer drug discovery. This study fabricated a chitosan-based scaffold combined with pectin at different ratios: 10:90, 40:60, 60:40, and 90:10. Collagen I, the most abundant component of breast cancer extracellular matrix (ECM), was added to the scaffold formula. The composite scaffold displayed an interconnected, open-pore structure with tunable porosity, swelling, and degradable characteristics at different chitosan-to-pectin ratios. A high ratio of chitosan to pectin (60:40 and 90:10) exhibited the ideal properties for a 3D scaffold suitable for cell culture. These scaffolds supported the attachment and growth of the T47D breast cancer cell line. Additionally, this 3D cell culture demonstrated doxorubicin and tamoxifen resistance when compared to 2D culture. Therefore, it is a feasible and promising tool for more reliable anticancer drug screening.

✉ Agustina Setiawati
nina@usd.ac.id

[1] Faculty of Pharmacy, Sanata Dharma University, Paingan, Maguwoharjo, Depok, Sleman, Yogyakarta 55282, Indonesia

[2] CURE 3D, Department of Cardiac Surgery, University Hospital Düsseldorf, 40225 Düsseldorf, North Rhine-Westphalia, Germany

[3] Laboratory of Macromolecular Engineering, Department of Pharmaceutical Chemistry, Faculty of Pharmacy, Universitas Gadjah Mada, Sleman, Yogyakarta 55281, Indonesia

[4] Laboratory of Advanced Pharmaceutical Sciences, Faculty of Pharmacy, Universitas Gadjah Mada, Sleman, Yogyakarta 55281, Indonesia

Graphical abstract

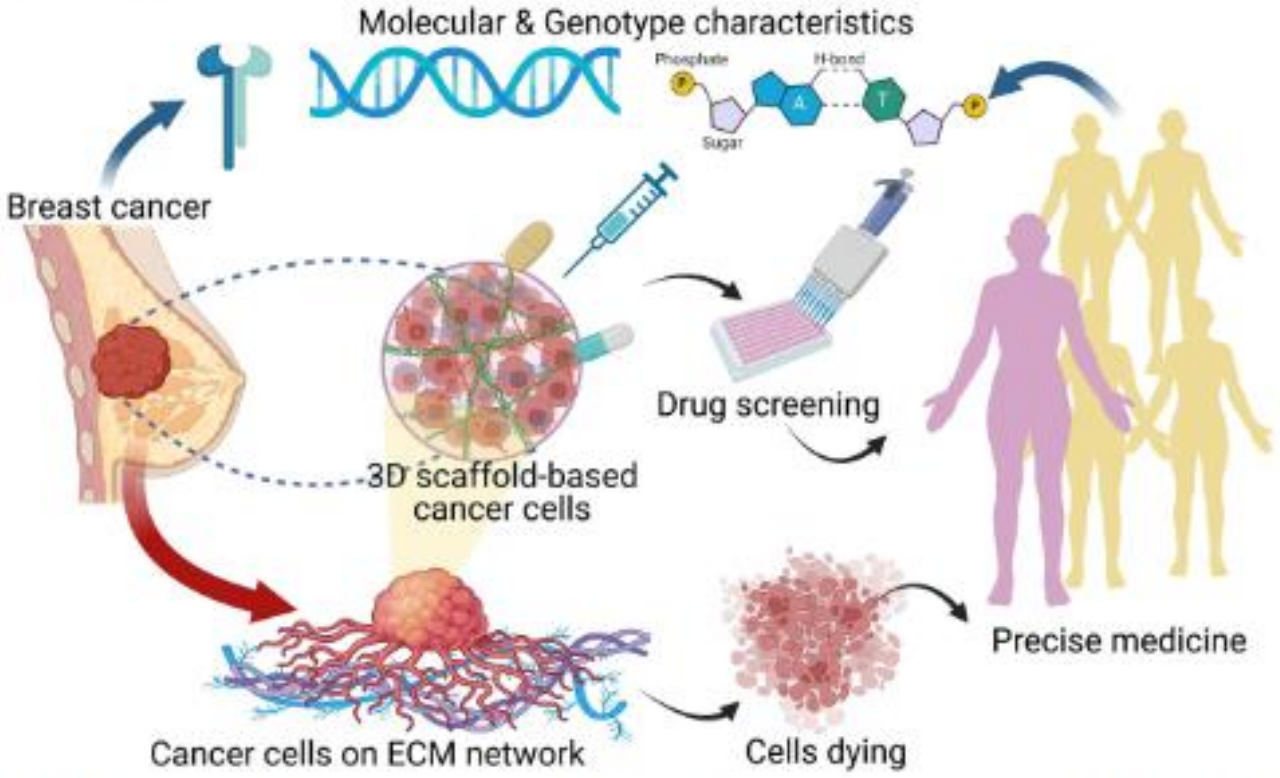

Biomimetic scaffold supports 3D growth of breast cancer cells. This system mimics breast cancer tissue which grows on ECM networks, offering a personalized and better model for anticancer drug screening.

Keywords Composite · High throughput screening · Drug discovery · Cancer · Polymer

1 Introduction

Even though massive resources have been allocated to cancer prevention, cancer remains the second leading cause of premature death [1]. According to recent global statistics, there will be roughly 10 million cancer-related deaths and nearly 20 million new cases of cancer in 2022. Demographics-based data indicate that by 2050, there will be 35 million new cases of cancer annually, a 77% increase from the 2022 profile [2]. Among them, breast cancer is the most frequently diagnosed cancer worldwide, and has been declared a global health burden by the World Health Organization (WHO) [2, 3]. As more individuals are being diagnosed with cancer every year, it continues to have a major impact on the number of cancer deaths worldwide [2, 4]. Given the growing need for efficient cancer treatments globally, significant progress in cancer treatment has been made over the past 50 years through extensive research [5]. Over the past 20 years, anticancer agent discovery has evolved from conventional cytotoxic drugs to immune-related and targeted therapies [6]. However, only around 10% of potential anticancer drugs reach the clinical stage, and the majority, nearly 97%, failed to obtain FDA approval [7, 8]. Anticancer drug discovery faces a persistently high attrition rate in the final stages of clinical development, making it one of the most challenging and high-risk areas in drug development [6]. The poor performance of early-stage anticancer drug development is attributed to shortcomings in translating preclinical in vitro and in vivo models to humans [6, 8].

Two-dimensional (2D) cell culture (also known as monolayer culture), commonly employed in high-throughput screening for in vitro anticancer drug candidate screening, lacks cell–cell and cell–extracellular matrix (ECM) interactions, leading to failure to mimic the tumor microenvironment [9, 10]. This limitation of 2D cell culture techniques is considered the major contributor to a high number of drug failures during the drug discovery process [11]. To mimic the tumor microenvironment, three-dimensional (3D) cell culture technology has become the next frontier in anticancer drug screening as it recapitulates the in vivo characteristics of tumor tissue [10, 12, 13]. Cancer cells are commonly cultured in a 3D matrix to behave more closely like those in tumor tissue [14]. These

3D cultures provide more physiological mimicry of the tumor microenvironment and exhibited notably elevated self-renewal abilities, cell malignancy, and drug resistance [14–16]. Therefore, significant efforts have been committed to developing 3D cancer cell cultures to improve the efficacy of cancer drugs'high-throughput screening (HTS).

There are two techniques to grow cells in 3D: scaffold-based and scaffold-free 3D cell culture. Scaffold-based 3D cell culture is more commonly applied in cancer studies than scaffold-free 3D cell culture [17, 18]. Due to inconsistent formation, handling difficulties, lack of ECM components, and controversial biological relevance of scaffold-free systems, they are not regarded as excellent models for cancer studies [19, 20]. Consequently, extensive studies have focused on fabricating scaffolds from natural or synthetic polymers or their combination with varying consistencies between hydrogel and porous forms. Although synthetic polymers like poly (lactide-co-glycoside) (PLGA), poly (2-hydroxyethyl methacrylate) (PHEMA), and polycaprolactone (PCL), have also been explored [21–23], they produce acidic degradation products that are harmful to cells and adversely affect experiment outcomes [14]. Therefore, natural polymers are more frequently used in tissue engineering due to their high biocompatibility than synthetic polymers. One of such natural polymers is chitosan, which has chemical structures similar to glycosaminoglycan, a key ECM constituent in the human body. It appears to be outstanding for producing 3D scaffolds for in vitro cell culture because it mimics a cancer cell's microenvironment [24, 25]. The interconnected open pore of the chitosan network, having a similar structure to native ECM, allows the cell to attach and proliferate [26, 27]. Previous studies reported that chitosan-based scaffolds support MCF- 7 breast cancer cells for drug screening application [28]. Despite its excellent characteristics as a scaffold, its mechanical weakness and instability make it difficult to maintain a set shape due to its swelling [29, 30]. Some studies have intensively developed chitosan composite with other natural polymers to enhance cell proliferation, reverse to a more malignant phenotype, and develop drug resistance [16, 30–33]. Chitosan/alginate scaffold effectively improved the biocompatibility and survivability of cancer stem cells and gliomas [14, 34]. Thus, its combination with hyaluronic acids is an ideal platform for a 3D glioma cell culture. [34]

To obtain an ideal scaffold for 3D cell culture, this study investigated the scaffold's microstructure, porosity, swelling, and degradation properties at different ratios of chitosan and pectin. Based on our findings, the ideal scaffold was further tested to grow T47D cells, which are positive estrogen receptor (ER)-expressing cells. Furthermore, a 3D ECM-based model was developed to evaluate doxorubicin and tamoxifen cytotoxicity in breast cancer cells. Using a 3D cancer model based on our chitosan/pectin/collagen I scaffold, it was demonstrated that doxorubicin and tamoxifen resistance phenomena occurred. Thus, this model provides valuable insights into the efficacy of anticancer drugs, which aligns with current trends in breast cancer research with a specific focus on studying hormone receptor interactions to develop targeted therapies.

2 Experimental

2.1 Materials

Blue swimming crab (*Portunus pelagicus*) shells, as a chitosan source, were harvested from Jepara, Central Java, Indonesia. Commercial pectin (P9135), bovine skin collagen (C4243), pluronic F127 (P2443), sodium dodecyl sulfate (436143), and paraformaldehyde (15817) were obtained from Sigma. Phosphate-buffered saline (PBS) (10010 - 023) was also purchased from Gibco. Cell viability number was assessed using 3-(4,5-dimethylthiazol-2-yl)− 2,5-diphenyltetrazolium bromide (MTT) from Invitrogen (M6494). Hydrochloric acid (HCl) (100317) and sodium hydroxide (NaOH) (106498) were obtained from Merck, respectively. For cell culture, T47D cells were propagated in 1% penicillin–streptomycin (Gibco, 10378016) and 10% Fetal Bovine Serum (FBS, Gibco 16000044) in Dulbecco's Modified Eagle's Medium (DMEM, Gibco). All well plates, glassware pipettes and used in all experiments were procured from Biologix, Pyrex, and SPL Life Sciences.

2.2 Chitosan isolation from *Portunus pelagicus*

Portunus pelagicus crab shells were sorted and washed in demineralized water. Cleaned shells were further dried in the oven at 50 °C for 2–5 days, the dried shells were powdered. The isolation process of chitosan consists of three main steps: deproteination, demineralization, and deacetylation as reported in previous research with little modifications [26, 27]. To extract the proteins from the sample, 15 g of crab shell powder was mixed with a 5% NaOH solution at a 1:10 (w/v) ratio. For 4 h, the mixture was cooked in a water bath between 80 and 90 °C while being stirred periodically. A 400-mesh nylon filter was then used to filter it, and the filtrate was washed with distilled water until the pH was neutral. After filtering, the solid was dried for 24 h at 50 °C in an oven. To remove minerals, the deproteinated shell powder was added with 1.5 N HCl at a 1:15 (w/v) ratio agitated continuously at room temperature for 2 h and then filtered using a 400-mesh nylon filter. To facilitate the deacetylation process, the demineralized shell powder was treated with 50% NaOH at a 1:10 (w/v) ratio, continuously stirred, and maintained at

80–90 °C for 4 h. The mixture was filtered again using a 400-mesh nylon filter, rinsed with demineralized water to neutralize the pH, and subjected to thermal drying at 50 °C for 24 h. Subsequently, Fourier Transform Infrared (FTIR) Spectroscopy was applied to investigate the specific chemical bonds present in chitosan within a spectral range of 400–4000 cm^{-1} with a resolution of 16 cm^{-1}.

2.3 Chitosan molecular weight determination

Chitosan's molecular weight is calculated based on a previous study [35]. The viscosity-average molecular weight of chitosan was determined using an intrinsic viscosity ([η]) measurement and the Mark-Houwink equation. Chitosan was dissolved in 0.1 M acetic acid at a 0.1 mg/mL concentration. The viscosity of the chitosan solution was measured at 25 °C using a capillary viscometer.

$$[\eta_r] = \frac{t_1}{t_0} \tag{1}$$

$$[\eta_{sp}] = \frac{t_1 - t_0}{t_0} = \frac{t_1}{t_0} - 1 = \eta_r - 1 \tag{2}$$

$$[\eta_{red}] = \frac{\eta_{sp}}{c} \tag{3}$$

$$[\eta_{inh}] = \frac{\ln \eta_r}{c} \tag{4}$$

The intrinsic viscosity (η) was determined by plotting reduced viscosity (η_{red}) and inherent viscosity (η_{inh}) against chitosan concentration (c). Linear regression ($y = ax + b$) provided intercepts (b) by extrapolating c to zero. The average of these intercepts was used as the intrinsic viscosity.

$$[\eta] = \lim_{c \to 0} \eta_{red} \tag{5}$$

$$[\eta] = \lim_{c \to 0} \eta_{inh} \tag{6}$$

The polymer's specific volume influences intrinsic viscosity (η). Which is linked to its molecular weight and interactions with the solvent. The connection between intrinsic viscosity (η) and the viscosity-average molecular weight (M_v) is described by the Mark-Houwink equation. The constants K and a are specific to a given polymer–solvent system at a particular temperature.

$$[H] = KM_v^a \tag{7}$$

2.4 Scaffold fabrication

Scaffolds were fabricated with various formulas based on crab shell chitosan: pectin ratio at 10:90 (F1), 40:60 (F2), 60:40 (F3), and 90:10 (F4), while bovine collagen I (COL I) was added at 0.010% concentration. Chitosan, pectin, and COL I were dissolved in 2% acetic acid (v/v), respectively. After being mixed, 25% glutaraldehyde was added to the solution until the final concentration was 1.2% (v/v) of the total solution. Subsequently, the homogeneous mixture was cast into a silicone mold with a size of 10 × 10 × 10 mm and frozen for 24 h at − 80 °C. Thus, the sample was freeze-dried for another 24 h.

2.5 FTIR confirmation of engineered scaffold

To investigate the functional group of chitosan, this study employed Attenuated Total Reflectance Fourier-Transform Infrared (AT-FTIR) using a spectral range of 400–4000 cm^{-1} with a resolution of 16 cm^{-1} and 100 scans.

2.6 Porosity test

The liquid displacement method was employed to investigate the scaffold porosity. After submerging the scaffold in anhydrous alcohol, excess ethanol was gently removed from its surface. The initial weight of the dried samples was marked as W0, whereas the weight measured after immersion was denoted as W1. Three replicates from each group were investigated, and the scaffold porosity was calculated using the following formula:

$$Porosity\ (\%): \ \frac{W1 - W0}{\rho \times V} \times 100\% \tag{8}$$

2.7 Scaffold morphology analysis

Scanning Electron Microscopy (SEM) (JEOL JSM7100 F) was used to observe and analyze the morphology of the Chitosan/Pectin/Collagen I scaffold, including surface topography. The composite scaffolds were sliced into transversal and vertical cross-sections before being placed on an aluminum sample metal disk with carbon tape and coated with gold. The images were captured at 50 × and 250 × magnification. Image-J was used to measure the pore size.

2.8 Swelling test

The dried scaffolds were originally submerged in PBS at 37 °C (W0). The scaffolds were taken out of the fluid after 1, 3, 6, 12, and 24 h of incubation. Before weighing (W1), the excessive PBS on the scaffold superficial was thoroughly cleaned

away [33]. The swelling ratio has been determined using the following formula:

$$Swellingratio\ (\%)\ :\ \frac{W1-W0}{W0}\times 100\% \tag{9}$$

2.9 Degradation test

The dried scaffolds (W0) were soaked in a PBS solution at 37 °C for 1, 3, 5, 24, and 72 h. The samples were removed and dried in an oven (W1) at the end of each incubation period. The ratio of degradation was determined using the following equation:

$$Degradation\ ratio\ (\%)\ :\ \frac{W0-W1}{W0}\times 100\% \tag{10}$$

2.10 Cell binding and viability test to scaffold

The T47D breast cancer cells were propagated in flasks supplemented with 10% FBS and 1% penicillin–streptomycin in DMEM at 37 °C in a 5% CO_2 atmosphere. After achieving confluence, cells were cleaned with PBS and spitted for 4 min in DMEM supplemented with 0.25% trypsin–EDTA. The collected cells were centrifuged at 1000 rpm for 3 min using an Eppendorf 5810R. A total of 5×10^5 cells were seeded onto scaffolds (F3 and F4) within a 24-well culture plate, utilizing a solution containing 5% Pluronic-F127 and deionized water for a 30-min incubation. Following a 6 h attachment period, the scaffolds were transferred into a fresh culture medium within a newly prepared 24-well plate, allowing further proliferation. To assess cell viability, tetrazolium salt (MTT) was added to the medium at 24-, 48-, and 72 h post-incubation, and the cells were maintained at 37 °C for 4 h. The resulting formazan crystals were then relocated into a separate 96-well plate and dissolved in 10% SDS, after which optical density was measured at 450 nm using a PerkinElmer multi-plate reader. Additionally, for scanning electron microscopy (SEM) analysis, the samples were initially fixed with 4% paraformaldehyde and subsequently subjected to a stepwise dehydration process involving ethanol concentrations of 30%, 50%, 70%, 90%, 96%, and 100%.

2.11 Cytotoxic evaluation of doxorubicin and tamoxifen using scaffold system

T47D cells (5×10^5) were seeded on the scaffold (F3 and F4) in a Pluronic-F127 coated 24-well plate. Following a 6-h incubation period, the scaffolds were moved to fresh media in a new 24-well plate. Doxorubicin (0.1, 0.5, and 1 µM) or tamoxifen (10, 50, and 100 µM) were treated in the cells for 72 h. Subsequently, the medium is transferred and replaced with new media containing 0.2 mg/mL MTT. The scaffolds in the well plate were then gently shaken, and 200 µL media was placed into a 96-well plate. A 10% SDS solution was added to dissolve the formazan complex. The absorbance was measured with an ELISA plate reader at a wavelength of 450 nm.

2.12 Statistical analysis

The quantitative data are displayed as means ± standard deviations, calculated from at least three independent measurements. Before analysis, outliers in the collected data were eliminated through preprocessing. One-way ANOVA was applied for statistical analysis, and Origin 9.0 was employed to report significance as $^*p < 0.05$ after the Tukey test.

3 Results and discussion

This study successfully engineered a scaffold-based 3D cell culture platform using chitosan, pectin, and collagen I composite with the addition of glutaraldehyde as a crosslinker (Fig. 1). Chitosan, a copolymer of glucosamine and N-acetyl glucosamine, is renowned for its excellent biocompatibility and biodegradability [36–38]. We used chitosan isolated from the *Portunus pellagicus* shell, which exhibited superior degradation characteristics [27]. Due to its poor swelling capacity and low mechanical properties, chitosan is combined with pectin to improve its swelling capacity and mechanical performance [39]. Hence, glutaraldehyde was introduced to enhance its stability in an aqueous environment [40, 41]. Moreover, collagen I was added to mimic breast cancer tissue and provide physical support for tissues [42, 43].

This study isolated chitosan from the *Portunus pellagicus* shell based on our previous studies [26, 27], yielding 12.17 ± 0.37%, respectively. The molecular weight of our isolated chitosan was 1691.65 kDa, likely indicating consistent mechanical and physical properties. Since the scaffold is intended for a drug screening model, the consistency of these properties is reflected in the pattern of porosity, swelling, and degradation ratio of the fabricated scaffold which is presented in the scaffold's characteristic results. Additionally, the isolated chitosan exhibited a degree of deacetylation (DD) of 70.34, which is considered high and indicates a greater number of amino groups, making it more water-soluble. This calculation is based on the absorption bands at 1320 cm^{-1} and 1420 cm^{-1}, which represent the acetylated amine or amide group in FTIR spectra (Supplementary 1), while the second band acts as the reference band [44].

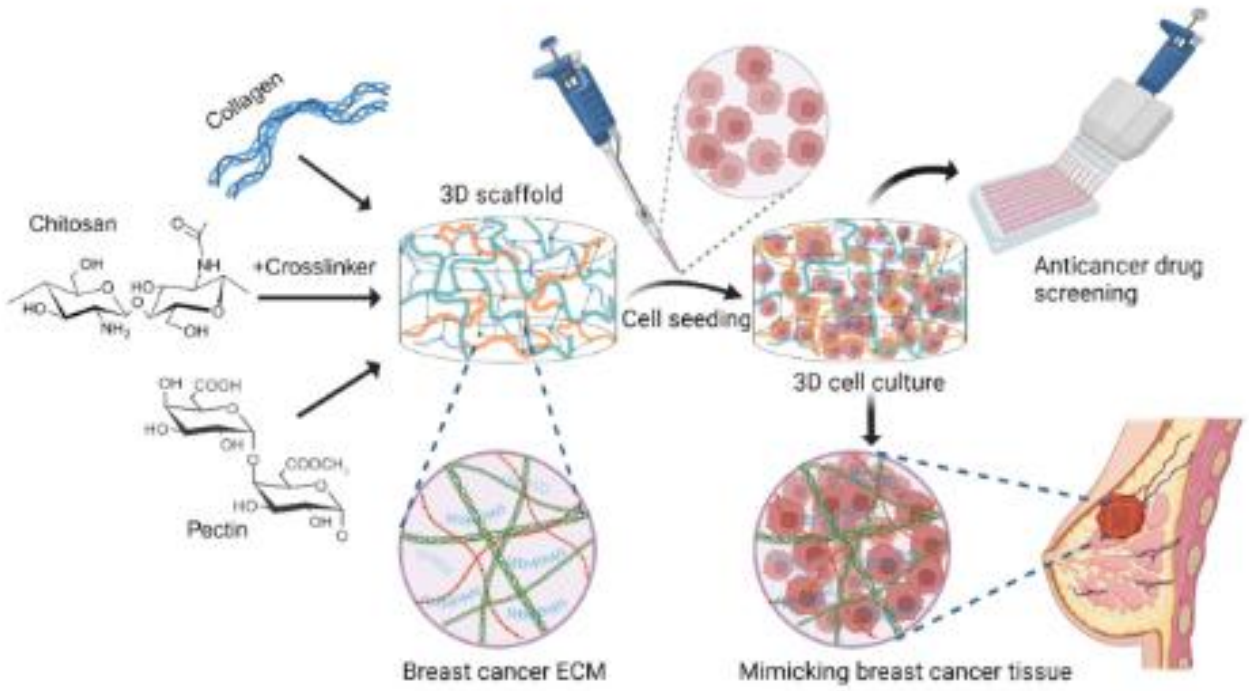

Fig. 1 Scheme of chitosan-based 3D scaffold fabrication to breast cancer tissue model for anticancer drug screening

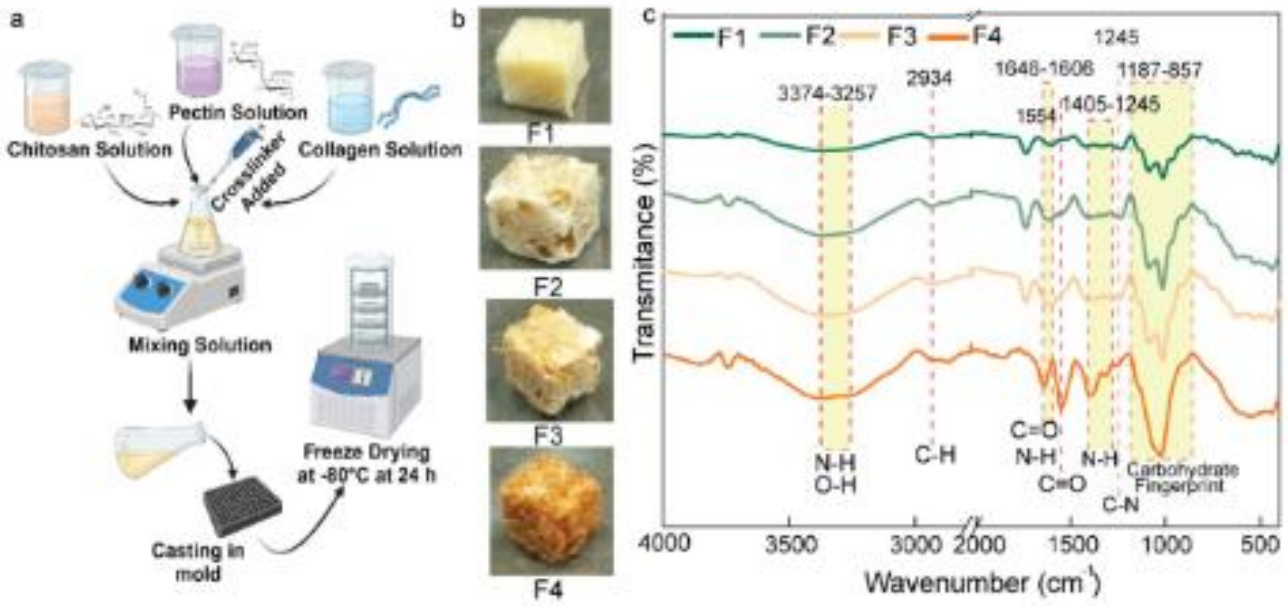

Fig. 2 The fabrication of chitosan-based composite. **a** Scaffold fabrication scheme, **b** Macroscopic morphology of fabricated scaffold with various formulas, **c.** FTIR spectra of various formulas (F1, F2, F3, F4) of fabricated scaffold

3.1 Scaffold fabrication and FTIR composition confirmation

We fabricated the scaffold using chitosan, pectin, and collagen I with a crosslinking agent, glutaraldehyde, using a facile method (Fig. 2a). The composite solution was prepared in an acidic solution with a pH range of 3 to 4 by dissolving chitosan, pectin, and collagen I in acetic acid, which was subsequently cast and freeze-dried to form a solid 3D scaffold. This study employed various scaffold formulas by

mixing chitosan and pectin in ratios of 10:90 (F1), 40:60 (F2), 60:40 (F3), and 90:10 (F4). The engineered scaffold presented a macroscopic porous structure with an off-white color at low proportion of chitosan (F1 and F2), while it turned darker in high proportion of chitosan (F3 and F4) (Fig. 1b). By employing freeze-drying, a chitosan/pectin/collagen I scaffold was successfully fabricated with high reproducibility, exhibiting an off-white color (F1) that darkened with a higher ratio of chitosan (F2 to F4). The composites crosslinked with glutaraldehyde had a brownish/orange color indicating the covalent bonding between glutaraldehyde and chitosan amine groups, where most aldols were transformed into enals or α,β-unsaturated imines [45, 46]. Our designed scaffold provides an interconnected structure that facilitates the transport of essential nutrients and the removal of metabolic byproducts within tumor-mimicking tissue. The interlinked network structure is most likely attributed to the bonding of amino groups in chitosan, pectin, and collagen I.

To confirm the success of the fabrication process, we conducted an FTIR experiment to identify the functional groups of the scaffold components. All the scaffold formulas revealed identical peak patterns from 4000 to 400 cm^{-1}. The band of OH and NH stretching broadly appeared at 3374–3257 cm^{-1}, attributed to intra- and intermolecular hydrogen bonds [47]. The OH group represents all components of the scaffold: chitosan, pectin, and collagen I while the NH group corresponds to chitosan and the amide a peak of collagen I molecules [47, 48]. Thus, the crosslink between chitosan and glutaraldehyde was also reflected by the double peaks at about 3300 cm^{-1}. Moreover, an absorption band at 2934 cm^{-1} exhibited an asymmetrical C-H stretch of the -CH_2 group [47]. Furthermore, the amide I and II peaks appeared at 1646 and 1606 cm^{-1}, respectively. The peak at 1405–1245 cm^{-1} was predicted to correspond to the C-N stretching of collagen, including both fibrillar and nonfibrillar collagen, with a range from 1100 to 1400 cm^{-1} [49]. The polysaccharides' fingerprint exhibited a distinct infrared spectrum in the 1187–857 cm^{-1} range due to variations in the glycosidic link structure in chitosan and pectin. The carbohydrate fingerprint peak was observed at 1187 cm^{-1} as a C–O–C bridge, which is referred to as the glycosidic band. The peak of C–C/C–O stretching was detected at 1087 and 1014 cm^{-1} in all the scaffold formulas. Thus, our study successfully identified specific peaks of chitosan and pectin as a carbohydrate polymer: Region II Peak of 1200–800 cm^{-1}) for the stretching vibration of C–C/C–O, Region IV (3050–2800 cm^{-1}) for the stretching vibrations of CH/CH_2, and Region V (3600–3050 cm^{-1}) for the stretching vibrations OH [44].

3.2 Scaffold microstructure and porosity

To mimic the ECM architecture of breast cancer tissue, the engineered structure must have a porous structure to allow cell attachment, distribution, and migration, as well as nutrient and waste transport to and from the scaffold [50]. This study applied an SEM investigation to observe the microstructure of the fabricated scaffolds (Fig. 3a). All the engineered scaffolds exhibited porous structures in both their surface and inner parts, with a wide range of pore diameters ranging from 26 to 250 µm. Our scaffold is constructed from interconnected chitosan, pectin, and collagen,

which forms a network that allows the synthetic tissue to transfer waste products and nutrients. Chitosan's amino groups, which establish connections with pectin and collagen, are most likely responsible for the successful connectivity of the mesoporous structure. There was no statistically significant difference in diameter between the F1 and F4 scaffolds. As shown in Fig. 1b, the pore diameters of F1, F2, F3, and F4 scaffolds were 55.92 ±27.82, 77.53 ±39.74, 94.67 ±54.051, and 162.66 ±93.76 µm, respectively. This suggests that the pore diameter of the scaffold increases with a higher proportion of chitosan. Moreover, this study investigated scaffold porosity, which is crucial for mass transfer during cancer cell proliferation [51]. According to the liquid displacement method, the porosity of F1 was 60.16 ±3.77%, respectively, statistically higher than the value of 43.88 ±10.61% for F2 ($p < 0.05$), 48.06 ±1.76% for F3 ($p < 0.05$), and 38.84 ±3.28% for F4 ($p < 0.01$). At the highest ratio of chitosan, the F4 scaffold exhibited the lowest porosity, significantly different from F3 (Fig. 3c). This was due to the decrease in the total porosity of the scaffold with a higher proportion of chitosan suggesting our isolated chitosan revealed consistent physical properties.

Aligning with our findings, previous studies have shown that an increase in chitosan content in the scaffold formula increased the pore diameter of the scaffold while maintaining or decreasing the porosity [52]. Similarly, another study on chitosan-coated polycaprolactone scaffolds reported enhanced mechanical properties and cell attachment with increased chitosan, but with a trade-off in porosity [23, 53]. Chitosan molecules create an open network structure allowing the formation of larger pores during freeze-drying [54]. Many studies have explained the correlation between chitosan proportion and porosity. A higher chitosan concentration occupies a higher volume fraction [55, 56]. Additionally, since chitosan has a high molecular weight, intrinsic density, and viscosity, it tends to occupy more space within the matrix and suppress bubble formation, leaving less room for pores [57]. Thus, an increased chitosan proportion leads to a higher crosslinked network with pectin and collagen, collapsing existing pores and reducing pore size [58, 59]. The denser matrix, due to the

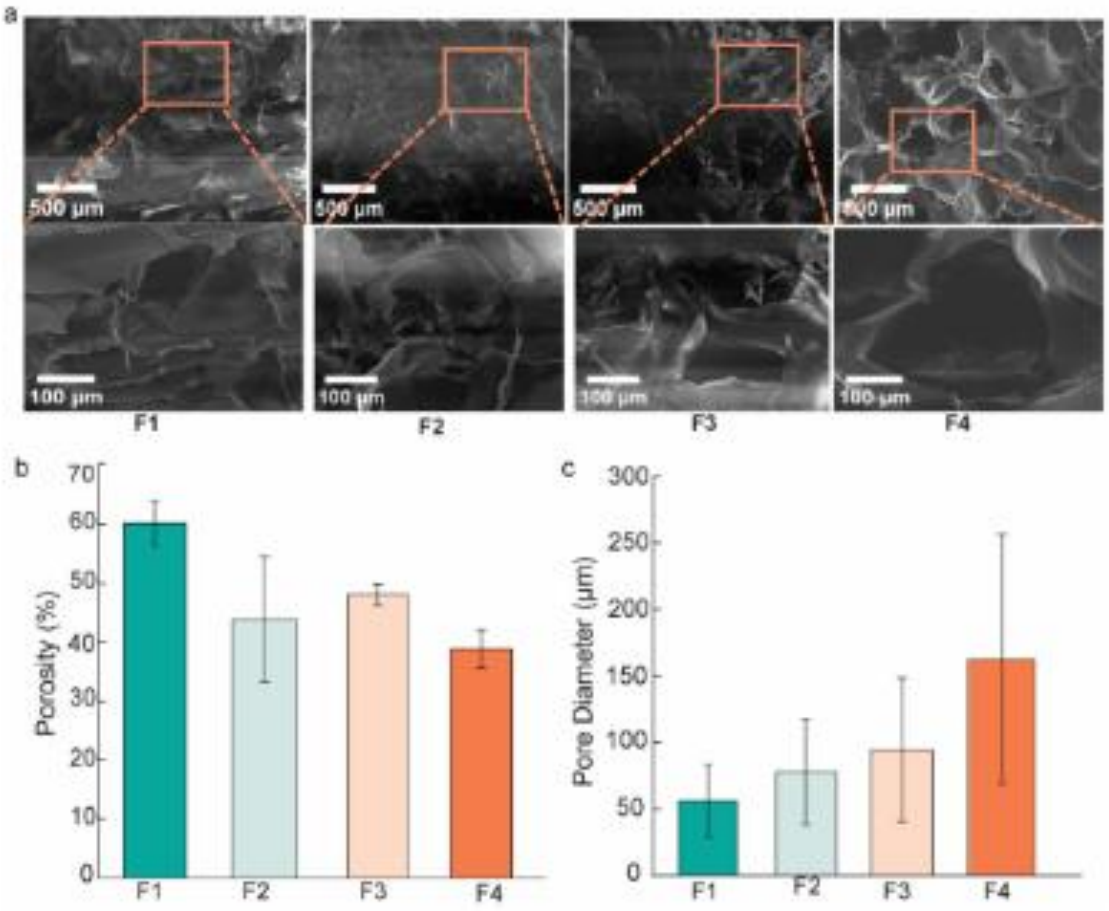

Fig. 3 Porous characteristics of the engineered scaffold. **a** Macroscopic porous architecture of various scaffold formulas under SEM. Upper images were observed at 50 magnifications, while bottom images were taken under 250 magnifications from the boxes of the upper area; **b** porosity analysis of each scaffold, $n = 5$; c. The pore diameter of each scaffold formula, $n = 5$. All quantitative data were presented in means ± SD. $^{*}p < 0.05$ and $^{**}p < 0.01$

higher concentration of chitosan, results from the chitosan molecules filling in the spaces between the pores, thereby reducing porosity by decreasing the total volume of voids within the scaffold [53, 60].

In general, the ideal pore size of scaffolds depends on the cell type and should be large enough to allow cells to attach and migrate through the structure [61]. Despite recent studies about pore size and its relationship with cell behavior, the optimum pore size remains debatable. The optimum pore diameter value is specific for each cell type [62]. There are previous studies investigating the pore size of 3D scaffolds for breast cancer cells. Since the diameters of all cells are less than 200 µm, a scaffold with a lower pore diameter was acceptable [63]. Pore size of more than 50 µm determines cell proliferation and colonization, while a range of 160–270 µm was found to be an ideal size for angiogenesis [64]. However, previous studies found that the optimal pore size for tissue engineering, especially in breast cancer models, is typically about 100 to 300 µm in diameter with 90% porosity [61, 65]. Thus, this is supported by Rijal and Li's study, which revealed that a pore size of about 100 µm was an ideal ECM matrix for growing 3D breast cancer cell culture [66]. These findings align with our study, in which F3 and F4 pore sizes of 94.67 ± 54.051, and 162.66 ± 93.76 µm were the most ideal scaffolds to grow T47D cells in 3D platforms.

3.3 The swelling and degradation ratio of the scaffold

The swelling capacity of the engineered scaffold demonstrated the ability of the scaffold to absorb water, including cell culture media, to supply nutrients for the cells to grow [41, 67]. The swelling behavior was investigated by

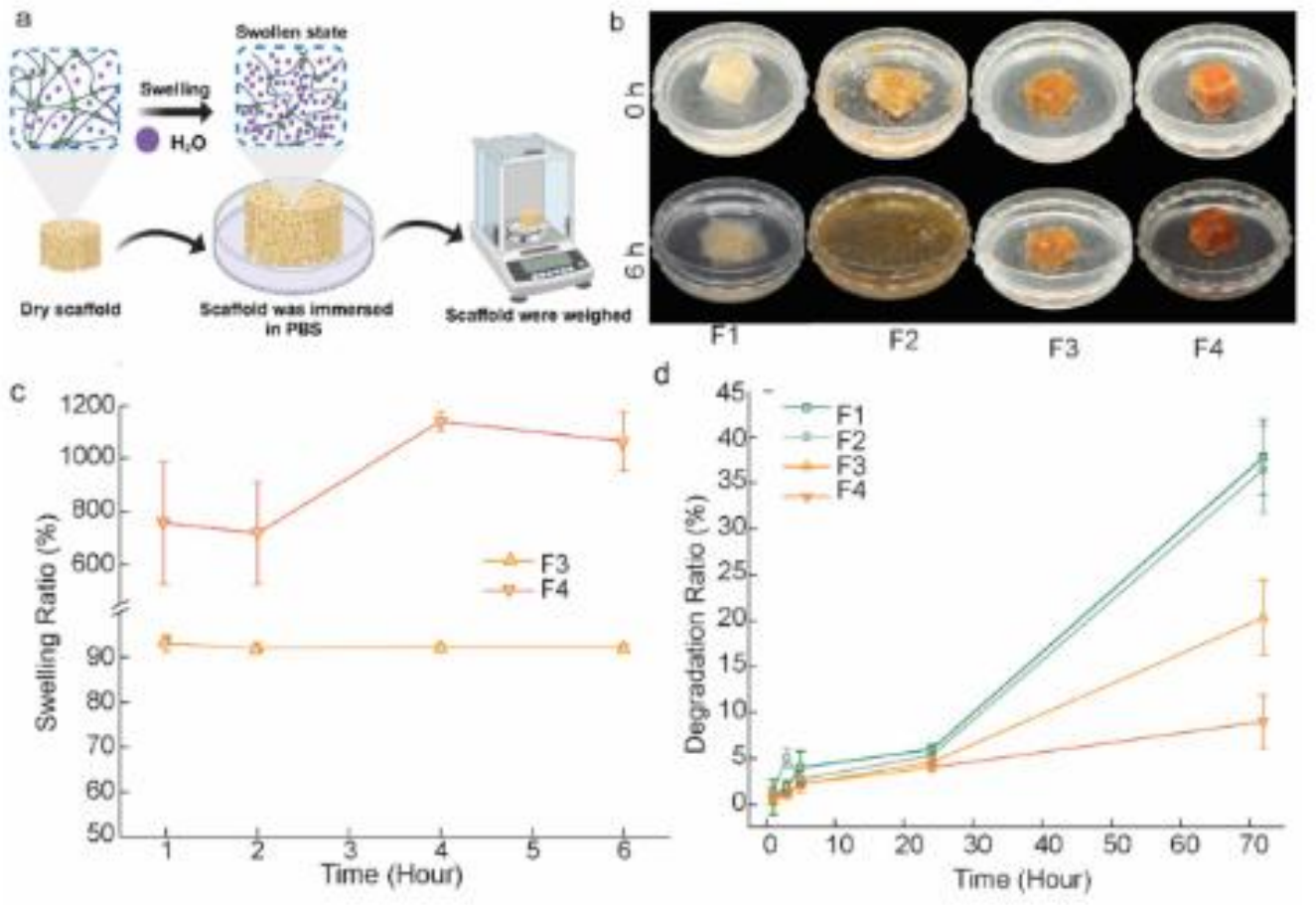

Fig. 4 Swelling and degradation characteristics of the fabricated scaffold. **a** Swelling scheme of, **b** Swelling of all scaffold formulas in PBS at 0 and 6 h, **c** Swelling ratio of F3 and F4 composite scaffold at 1, 2, 4, and 6 h, **d** Degradation ratio of all scaffold formulas in PBS at 30 min, 1, 2, 24, and 72 h. All quantitative data were presented in means ± SD ($n = 5$)

immersing the scaffolds in PBS at 37 °C. The degree of swelling was influenced by the movement of water through molecular interactions within the scaffold's structure, leading to an increase in its volume (Fig. 4a). This study evaluated swelling ratios for up to 6 h. F1 and F2 scaffolds were dissolved in PBS within 2 h, while F3 and F4 remained stable until 6 h (Fig. 4b). The swelling ratios of F3 were 91.20 ± 1.18%, 92.99 ± 1.74%, 92.22 ± 0.51%, and 92.16 ± 0.60% at 30 min, 1, 2, 4, and 6 h, respectively. Meanwhile, the swelling ratios of F4 over the same period were 804.86 ± 114.22%, 756.89 ± 232.22%, 718.66 ± 194.83%, 1140.23 ± 37.89%, and 1065.13 ± 112.28% (Fig. 4c). It was found that all scaffolds indicated that the chitosan proportion in the scaffold plays a crucial role in structural stability and swelling. The hydrophilic group of chitosan, such as –OH and $–NH_2$ groups absorb water molecules from PBS, resulting in a higher swelling capability of the scaffold [68]. The ideal swelling ratio for a scaffold varies based on the specific application and materials used. Excessive swelling may compromise structural integrity and the degradation rate, leading to potential failure in scaffolds designed for supporting tissue regeneration [69]. It also alters the microenvironment of the scaffold, affecting cell behavior, migration, and nutrient transfer. Excessive swelling could hinder cell attachment and proliferation. Swelling ratios typically range from 100 to 300%. Some studies have indicated that specific composite scaffolds can achieve swelling ratios as high as 600 to 1850%, depending on their composition and structure [70, 71].

Moreover, this study observed the degradation ratio of the scaffold for 72 h which is a suitable time frame for cytotoxic assay in anticancer drug screening. At 1, 3, 5, 24, 72 h, the degradation ratios of F1 scaffold were 0.81 ± 1.93%, 1.91 ± 0.62%, 3.99 ± 1.77%, 5.97 ± 0.51%, 37.77 ± 4.07%; meanwhile, the degradation ratios of F2 scaffold were 1.43% ± 0.52, 5.08 ± 1.04%, 2.72 ± 0.34%, 5.34 ± 0.77%, and 36.43 ± 4.72%. Conversely, the F3 scaffold demonstrated a distinct degradation ratio of 0.45 ± 0.29%, 1.24 ± 0.54%, 2.17 ± 0.40, 4.78 ± 0.38%, and 20.31 ± 4.12%, respectively. Similarly, the F4 scaffold revealed an average degradation ratio of 0.79

±0.22%, 1.12 ±0.23%, 2.19 ±0.89%, 3.99 ±0.29%, and 9.00 ±2.89% at the same incubation times (Fig. 4d). The statistically different degradation ratios were observed for F3 and F4 for 72 h of incubation. Along with the porosity and swelling ratio, scaffolds with higher chitosan proportion exhibited better structural stability, which was shown in a lower degradation ratio. These consistent results indicated that isolated chitosan showed constant physical properties in the fabricated scaffold. Therefore, this study further used F3 and F4 scaffolds for cell viability and cytotoxicity assays.

Chitosan contains abundant hydroxyl and amino groups, which enable it to facilitate water absorption and swell. However, at a lower proportion of chitosan compared to pectin, the scaffold may lack sufficient crosslinking and structural support, leading to increased solubility in water and scaffold degradability [72, 73]. With a higher proportion of chitosan compared to pectin, the composite scaffolds maintained their structure, thus revealing a higher swelling ratio than scaffolds with a lower chitosan ratio. The interconnected pore formed by chitosan crosslinking may facilitate water absorption, which results in a higher swelling ratio. The degree of swelling is influenced by the pore size and distribution, where a larger and interconnected network of pores tends to promote higher swelling ratios in F4 than in F3 [72, 74].

Moreover, scaffolds with higher chitosan content exhibited slower degradation properties. Enzymatic hydrolysis, mostly catalyzed by lysozymes, is the main approach by which chitosan is broken down within these scaffolds. Glycosidic linkages between the polysaccharide units in chitosan are broken during this process, forming smaller oligosaccharides like glucosamine and other saccharides that the body may use or break down [75, 76]. The degree of chitosan deacetylation (DD) affects the rate of enzymatic breakdown; a higher DD leads to slower degradation rates because of increased crystallinity [76, 77]. Additionally, previous work reported that pectin was primarily degraded by enzymes, particularly by pectinases produced by gut microbiota or other microorganisms. These enzymes cleave the glycosidic bonds within the pectin polymer, resulting in smaller oligosaccharides and monosaccharides [78, 79]. Similarly, collagen fibers are broken down by collagenases into smaller peptides and amino acids [80]. Chitosan slowed down the degradation process of the composites due to its more stable structure than pectin [81]. Therefore, scaffold with a higher ratio of chitosan to pectin (60:40 and 90:10) were used for the biofunctionality test.

3.4 T47D cell attachment and growth to the scaffold

Since the scaffold is intended to be used as a 3D cell culture for more reliable anticancer drug screening, this study investigated the functionality of the scaffold by seeding the T47D breast cancer cell line onto the F3 and F4 scaffold. This study assessed the cell viability by measuring the absorbance of formazan, the product of tetrazolium salt due to succinic dehydrogenase in living cells at 450 nm. [81] Before the drug treatment, well plates were coated with Pluronic F127 to avoid cell attachment to the bottom [82]. Samples F3 and F4 supported cell attachment and viability, with the absorbance readings at 450 nm measured until 96 h. Since a cytotoxic assay typically does not need to exceed 72 h, this study assessed the ability of the scaffold to support cell viability for 72 h. F3 supported breast cancer cells with average absorbance values of 0.305 ±0.00, 0.205 ±0.01, and 0.204 ±0.00 for 24, 48, and 96 h of incubation time. In contrast, F4 supported a significantly higher number of T47D cells ($p < 0.01$) at each incubation time, with absorbance values of 0.983 ±0.01, 1.749 ±0.04, and 1.81 ±0.08, respectively (Fig. 5b). The cells were well distributed and occupied the interior of the scaffold's pore rather than the scaffold surface within the first 24 h, exhibiting a round shape morphology rather than the flat shape typically observed in 2D cultures (Fig. 5c). Furthermore, the microscopic pore of the scaffold changed due to cell occupation and growth. Thus, cells secreted their own ECM and remodeled the scaffold to form fibrillar ECM surrounding their microenvironment (Fig. 5d). This observation may explain the reciprocal interaction between cells and the scaffold, which is crucial for the success of tissue engineering [82]. The density and organization of collagen fibers modulated how T47D cells interacted with their microenvironment, impacting growth and invasive potential [83, 84]. A higher collagen matrix is associated with a stiffer ECM, promoting malignant transformation and enhanced cell migration [83]. Thus, the stiffness of the collagen matrix also plays a critical role, with denser matrices promoting more aggressive growth patterns in response to hormonal signaling, especially estrogen and prolactin in T47D cells. [84]

3.5 Doxorubicin cytotoxic evaluation in 3D T47D cells culture

To investigate the scaffold's ability for breast cancer cell screening, this study compared the cytotoxic assay of doxorubicin and tamoxifen using a 2D flat surface and the selected scaffold (F3 and F4) in T47D cells. Doxorubicin and tamoxifen are chemotherapeutic agents of choice to treat breast cancer patients. Doxorubicin treatment exhibited dose-dependent effects on T47D cells in the 2D culture, F3, and F4 scaffold 3D system at concentrations of 0.1, 0.5, and 1 μM. Under 0.1 μM doxorubicin treatment, the cell viabilities of the 2D culture, F3, and F4 scaffold group were 73.03 ±8.31%, 77.33 ±1.81%, and 89.43 ±2.22%, respectively. When treated with 0.5 μM, the cell viabilities

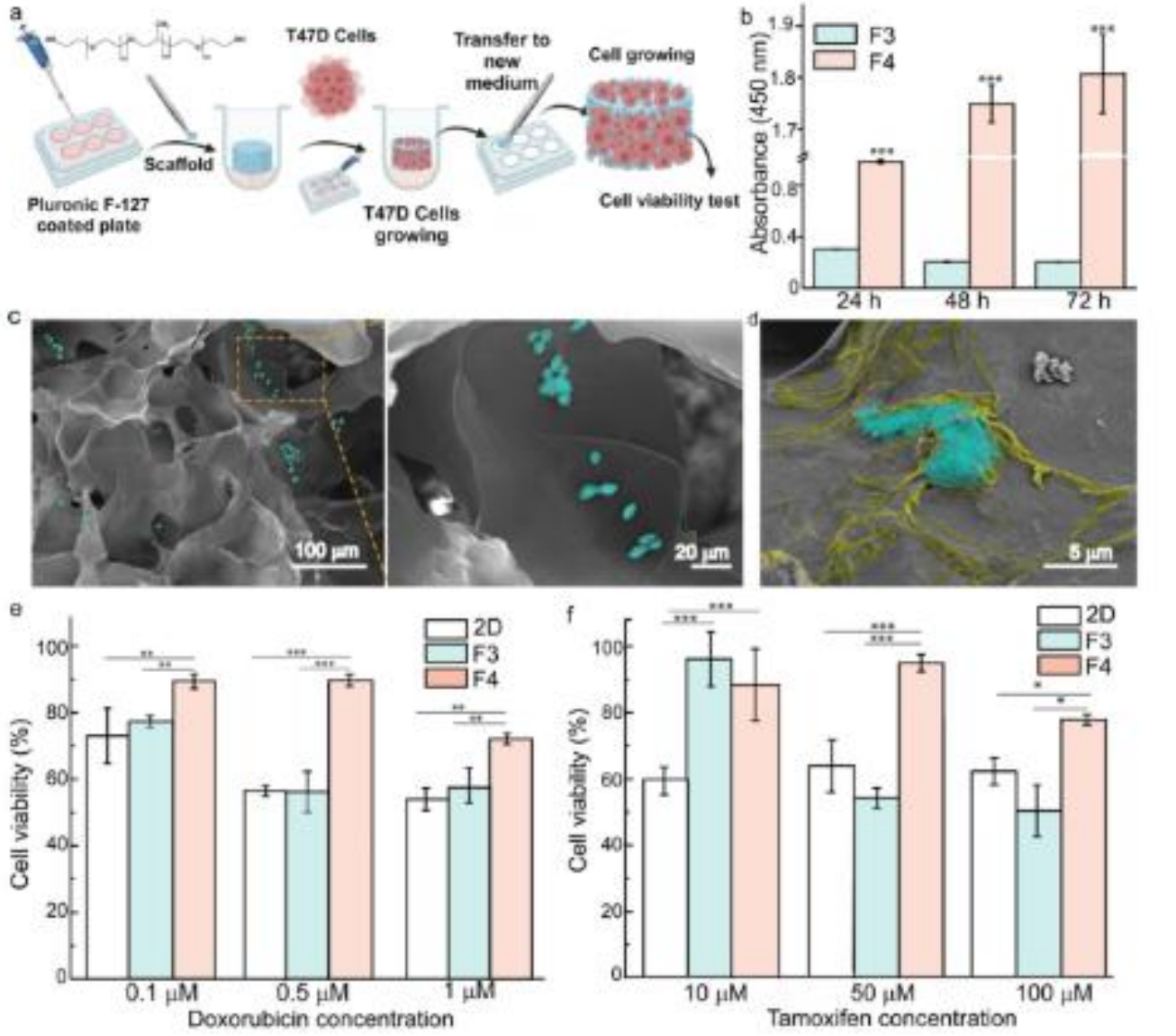

Fig. 5 Biofunctionality test of selected scaffold formula (F3 and F4) by seeding T47D breast cancer cells. **b** Absorbance profile at 450 nm after the cells were being treated to MTT. **c** T47D cell morphology inside of F4 scaffold's pore, **d** T47D cells' morphology in the scaffold after 72 h. Green represents the cells, yellow demonstrates ECM fibers, e. The cells' viability comparison among 2D culture, F3, and F4 scaffold after doxorubicin treatment, f. The cells' viability comparison among 2D culture, F3, and F4 scaffold after tamoxifen treatment. All quantitative data were presented in means ± SD ($n = 5$). Statistical significance was calculated using a one-way ANOVA followed by the Tukey test; $^{**}p < 0.01$, and $^{***}p < 0.001$

were 56.81 ± 1.51%, 56.21 ± 6.13%, and 89.71 ± 1.79% for the 2D culture, F3, and F4 scaffold groups. Moreover, the T47D cell viability in the 2D culture, F3 and F4 group were 53.54 ± 3.32%, 57.52 ± 5.29%, and 72.09 ± 1.55%, respectively, when cells were treated with 1 μM doxorubicin (Fig. 5e). T47D cells were more susceptible to doxorubicin in the 2D cell culture system and F3 scaffold than in the F4 scaffold with no statistical difference across all concentration levels. On the other hand, T47D cells exhibited phenomena resistance to doxorubicin in the F4 scaffold group, with significant differences compared to the 2D culture and F3 scaffold groups ($p < 0.01$ and $p < 0.001$).

It was observed that higher chitosan content enhanced biocompatibility and cancer cell bioavailability. Consistent with previous studies, chitosan in a composite improves biocompatibility and is likely to be selected as a promising candidate for a tissue engineering model [85]. Additionally, collagen I provides a binding domain for the α2β1 integrin receptor, which initiates focal adhesion signaling molecules, leading to cancer cell progression [42, 81, 86, 87]. Incorporating collagen I into the scaffold was found to be a

strategy with potential for enhancing cell adhesion. When T47D cells adhere to the scaffold, whether through chitosan or collagen I, they remodel the scaffold and secrete their own ECM [88], as observed in our data. Our chitosan-based scaffolds supported T47D cell attachment and proliferation; therefore, a cytotoxicity test using a chemotherapy agent was further required.

3.6 Tamoxifen cytotoxic evaluation in 3D T47D cells culture

To be applied in drug screening, tamoxifen was administered to the T47D cells, which are estrogen receptor-positive cells that are susceptible to both common chemotherapy, such as anthracyclines like doxorubicin, and an estrogen receptor inhibitor, such as tamoxifen [89]. Furthermore, this study also investigated the cytotoxicity of tamoxifen, an estrogen receptor alpha antagonist, on T47D cells in the selected scaffold (F3 and F4). This study investigated cell viability using concentrations of 10 to 50 µM at which T47D cells exhibited a cytotoxic effect rather than an estrogenic effect. At the lowest concentration (10 µM), the cells viability of the F3 and F4 groups was 96.14 ± 8.28% and 88.42 ± 10.88%, respectively. Both cell viabilities in those groups were significantly higher than those in 2D culture (59.47 ± 4.2%, $p < 0.001$), indicating that the cells were resistant to tamoxifen. However, the 2D culture and F3 group showed susceptibility to treatment with over 50 µM tamoxifen, with cell viability values of 63.46 ± 7.63% and 54.20 ± 3.00%, respectively. These values are significantly lower than the value of 94.97 ± 2.60% ($p < 0.001$) for the F4 scaffold, indicating tamoxifen resistance. Furthermore, after being treated with 100 µM, the cell viability for the 2D culture and F3 scaffold was 61.76 ± 3.99% and 50.35 ± 7.75%, respectively, which are statistically lower than 77.97 ± 1.59% for the F4 scaffold ($p < 0.05$) (Fig. 5f). Thus, T47D cells exhibited increased resistance when they grew in F4 scaffolds, which represent native breast cancer tissue-like microenvironments.

Doxorubicin and tamoxifen demonstrated significantly greater potency against breast cancer cells grown in 2D cultures compared to those cultured in a 3D scaffold-based model [90, 91], particularly in scaffolds with higher chitosan content. Not only did chitosan in the scaffold support T47D cell growth, but also Katz and colleagues revealed that collagen in the 3D scaffold also contributed to their resistance due to its ability to mimic the tumor microenvironment [90]. Thus, a study by Landberg and colleagues found that estrogen receptor breast cancer cells cultured in a patient-derived 3D matrix exhibited resistance to various chemotherapies including doxorubicin, fluorouracil, and paclitaxel [92]. Since environmental factors, such as tumor cell adhesion to stromal components, mediate de novo resistance [93–95], these findings suggest that our scaffold, which mimics the ECM, may strongly contribute to T47D resistance. Additionally, the F4 scaffold may create localized hypoxic conditions, which have been demonstrated to play a major role in cancer cells'drug resistance. Increased expression of anti-apoptotic proteins and metabolic changes that improve cell survival under stress can result from hypoxia's activation of hypoxia-inducible factors (HIFs) [11].Therefore, further studies on the hypoxia effect in the 3D cell culture system using our fabricated scaffold are warranted.

To sum up, a chitosan-based scaffold could be considered a cutting-edge strategy for precise high-throughput screening in anticancer drug discovery. By demonstrating that ER-positive breast cancer cells exhibit resistance in our scaffold model, this study provides valuable insights into the efficacy of anticancer drugs in a more clinically relevant context. Furthermore, it aligns with current trends in breast cancer research, which aims to study hormone receptor interactions for developing targeted therapies in precise medicine.

4 Conclusion

In this study, a biomimetic breast cancer microenvironment was successfully fabricated by combining *Portunus pelagicus* shell-derived chitosan, pectin, and collagen I used the freeze-drying method. The engineered composite scaffold exhibited an open pore interconnected network, resulting in cell attachment and colonization into the scaffold. Hence, the high content of chitosan in the composite provides swelling and degradation properties. Moreover, it supported the growth of ER-positive breast cancer cells; thus, the cells secreted their own ECM and remodeled the scaffold. Furthermore, T47D indicated resistance to doxorubicin and tamoxifen in a 3D chitosan-based scaffold than 2D culture. Thus, our fabricated scaffold is a promising and sustainable tool for anticancer drug screening.

Supplementary Information The online version contains supplementary material available at https://doi.org/10.1007/s13233-025-00405-7.

Author contributions A.Setiawati performed conceptualization, investigation, supervising experiments, and writing the whole manuscript; N.B.W. Kencana, M.V.S.A. Kencana fabricated and characterized the scaffold; H.S.D. Putra fabricated scaffold and data visualization, N.Fatimah, I.M.K. Yoga conducted a cell seeding experiment, O.Ajiteru performed data interpretation, manuscript proofreading, and editing; A.Hermawan supervised cell-related data and reviewed the manuscript.

Funding This study was conducted under Post Doctoral, Universitas Gadjah Mada with grant number 4292/UN1.P1/PT.01.03/2024. Thus, the chitosan isolation protocol was developed under the Fundamental

Scheme of the Internal Research Grant of Sanata Dharma University No.019 Penel./LPPM-USD/III/2024.

Data availability All the data resulted or analyzed during this study are included in the manuscript.

Declarations

Conflict of interest The authors declare no competing interests.

Ethical approval This study was conducted following the protocols approved by the Faculty of Health Sciences Ethics Committee, Respati University of Yogyakarta, Indonesia (Approval No. 052.3/FIKES/PL/V/2024).

Consent to participate Not applicable.

Consent for publication Not applicable.

References

1. F. Bray, M. Laversanne, E. Weiderpass, I. Soerjomataram, Cancer **127**(16), 3029 (2021)
2. F. Bray, M. Laversanne, H. Sung, J. Ferlay, R.L. Siegel, I. Soerjomataram, A. Jemal, CA Cancer J. Clin. **74**(3), 229 (2024)
3. L. Wilkinson, T. Gathani, Br. J. Radiol. **95**(1130), 7 (2022)
4. M. Arnold, E. Morgan, H. Rumgay, A. Mafra, D. Singh, M. Laversanne, J. Vignat, J.R. Gralow, F. Cardoso, S. Siesling, I. Soerjomataram, Breast **66**, 15 (2022)
5. J. Sun, Q. Wei, Y. Zhou, J. Wang, Q. Liu, H. Xu, BMC Syst. Biol. **11**, 28 (2017)
6. Z. Liu, B. Delavan, R. Roberts, W. Tong, TIPS. **38**(10), 852 (2017)
7. R. Mirzayans, D. Murray, Int. J. Mol. Sci. **23**(21), 13217 (2022)
8. S. Breslin, L. O'Driscoll, Drug Discov. Today **18**(5–6), 240 (2013)
9. D. Antoni, H. Burckel, E. Jossel, G. Noel, Int. J. Mol. Sci. **16**(3), 5517 (2015)
10. A.M.K. Law, L. Rodriguez de la Fuente, T.J. Grundy, G. Fang, F. Valdes-Mora, D. Gallego-Ortega, Front. Oncol. **11**, 1 (2021)
11. S.A. Langhans, Front. Pharmacol. **9**, 1 (2018)
12. M. Kapalczyńska, T. Kolenda, W. Przybyła, M. Zajączkowska, A. Teresiak, V. Filas, M. Ibbs, R. Bliźniak, Ł Łuczewski, K. Lamperska, Arch. Med. Sci. **14**(4), 910 (2018)
13. C. Jubelin, J. Muñoz-Garcia, L. Griscom, D. Cochonneau, E. Ollivier, M.-F. Heymann, F.M. Vallette, L. Oliver, D. Heymann, Cell Biosci. **12**, 1 (2022)
14. F.M. Kievit, S.J. Florczyk, M.C. Leung, O. Veiseh, J.O. Park, M.L. Disis, M. Zhang, Biomaterials **31**(22), 5903 (2010)
15. X. Wang, X. Dai, X. Zhang, X. Li, T. Xu, Q. Lan, BBRC. **498**(4), 1052 (2018)
16. A.E. Erickson, S.K.L. Levengood, J. Sun, F.-C. Chang, M. Zhang, Adv Healthc Mater. **7**(15), 1 (2018)
17. E.-T. Verjans, J. Doijen, W. Luyten, B. Landuyt, L. Schoofs, J. Cell. Physiol. **233**(4), 2993 (2018)
18. K. Unnikrishnan, L.V. Thomas, R.M.R. Kumar, Front. Oncol. **11**, 1 (2021)
19. J. Rashidian, K. Luo, Methods Mol. Biol. **1344**, 121 (2016)
20. B. Weigelt, M.J. Bissell, Adv. Drug Deliv. Rev. **67–70**, 42 (2014)
21. C. Fischbach, R. Chen, T. Matsumoto, T. Schmelzle, J.S. Brugge, P.J. Polverini, D.J. Mooney, Nat. Methods **4**(10), 855–860 (2007)
22. N. Tuancharoensri, S. Sonjan, S. Promkrainit, J. Daengmankhong, P. Phimnuan, S. Mahasaranon, J. Jongjitwimol, P. Charoensit, G.M. Ross, C. Viennet, J. Viyoch, S. Ross, Polymers **15**(20), 4052 (2023)
23. J. Sun, X. Liu, Z. Chen, L. Jiang, M. Yuan, M. Yuan, Materials **15**, 1591 (2022)
24. S.J. Florczsyk, K. Wang, S. Jana, D.L. Wood, S.K. Sytsma, J.G. Sham, F.M. Kievit, M. Zhang, Biomaterials **34**(38), 10143 (2013)
25. D. Lv, Z. Hu, L. Lu, H. Lu, X. Xu, Oncol. Lett. **14**(6), 6999 (2017)
26. A. Setiawati, K. Tricahya, F.D.O. Riswanto, Y. Dwiatmaka, J. Biomater. Sci. Polym. Ed. **35**(2), 146 (2024)
27. L.C. Devi, H.S.D. Putra, N.B.W. Kencana, A. Olatunji, A. Setiawati, Biomedicines **12**(8), 1 (2024)
28. H.K. Dhiman, A.R. Ray, A.K. Panda, Biomaterials **26**(9), 979 (2005)
29. D.R. Rohindra, A.V. Nand, J.R. Khurma, SPJNAS **22**, 32 (2004)
30. Z. Li, H.R. Ramay, K.D. Hauch, D. Xiao, M. Zhang, Biomaterials **26**(18), 3919 (2005)
31. S.A. Solimani, S. Irani, M. Mohamadali, H. Bakhshi, Appl. Biochem. Biotechnol. **195**, 7638 (2023)
32. A. Kabirkoohian, H. Bakhshi, S. Irani, F. Sharifi, Appl. Biochem. Biotechnol. **195**, 3888 (2023)
33. Z. Li, M. Zhang, J. Biomed. Mater. Res. A **75A**(2), 485 (2005)
34. S.J. Florczyk, F. Kievit, K. Wang, K. Erickson, J. Mater. Chem. B. **4**(38), 6326 (2016)
35. R. Czechowska-Biskup, R.A. Wach, J.M. Rosiak, and P. Ulański, *Prog. Chem. Appl. Chitin Deriv*. **23**,(8), 45-54 (2016).
36. H. Amiri, M. Aghbashlo, M. Sharma, J. Gaffey, L. Manning, S.M.M. Basri, J.F. Kennedy, V.K. Gupta, M. Tabatabaei, Nat Food **3**, 822 (2022)
37. M. Kmiec, L. Piginelli, M.F. Tedesco, M.M. Silva, V. Reis, J. Tissue Eng. Regen. Med. **2**, 205 (2017)
38. J. Venkatesan, S.K. Kim, Mar. Drugs **8**(8), 2252 (2010)
39. D. Demir, S. Ceylan, D. Göktürk, N. Bölgen, Polym. Bull. **78**, 2211 (2021)
40. H. Zhao, J. Liao, F. Wu, J. Shi, J. Mech. Behav. **114**, 104169 (2021)
41. N. Shanmugasundaram, P. Ravichandran, P.N. Reddy, N. Ramamurty, S. Pal, K.P. Rao, Biomaterials **22**(14), 1943 (2001)
42. C. Dong, Y. Lv, Polymers **8**(2), 1 (2016)
43. L.C.M. Ngoka, Proteome Sci. **6**, 1 (2008)
44. B. Fatima, Quantitative Analysis by IR: Determination of Chitin/Chitosan DD, (IntechOpen, London, 2020), pp. 1–24
45. L.A. Sawicki, L.H. Chloe, K.L. Wiley, K.H. Lee, A.M. Kloxin, A.C.S. Biomater, Sci. Eng. **4**(3), 836 (2018)
46. A. Arianita, Cahyaningtyas, B. Amalia, W. Pudjiastuti, S. Melanie, V. Fauzia, and C, Imawan 2019 J. Phys Conf. Ser. https://doi.org/10.1088/1742-6596/1317/1/012045
47. J. Becerra, M. Rodriguez, D. Leal, K. Noris-Suarez, G. Gonzalez, J. Mater. Sci. Mater. Med. **33**(2), 18 (2022)
48. T. Riaz, R. Zeeshan, F. Zarif, K. Ilyaz, N. Muhammad, S.Z. Safi, A. Rahim, S.A.A. Rizvi, I.U. Rehman, Appl. Spectrosc. Rev. **53**(9), 703 (2018)
49. R. Pallela, J. Venkatesan, V.R. Janapala, S.K. Kim, J. Biomed. Mater. Res. A **100**(2), 486 (2012)
50. M.S. Flores-Jiménez, A. Garcia-Gonzalez, R.Q. Fuentes-Aguilar, A.C.S. Appl, Bio Mater. **6**, 1 (2023)
51. G. Rijal, W. Li, J. Biol. Eng. **12**, 1 (2018)
52. M. Jafarkhani, A. Fazlali, F. Moztarzadeh, and M. Mozafari, *Iran. Polym. J*., **21**, 713–720 (2012)
53. A. Ressler, Polymers **14**, 3430 (2022)
54. G. Harini, R. Bharathi, A. Sankaranarayanan, A. Shanmugavadivu, N. Selvamurugan, Mater. Adv. **4**, 3907 (2023)
55. M.W. Tibbitt, K.S. Anseth, Biotechnol. Bioeng. **103**(4), 655–663 (2009)
56. X. Wu, Y. Liu, X. Li, P. Wen, Y. Zhang, Y. Long, X. Wang, Y. Guo, F. Xing, J. Gao, Acta Biomater. **6**(3), 1167–1177 (2010)
57. T. Ikeda, K. Ikeda, K. Yamamoto, H. Ishizaki, Y. Yoshizawa, K. Yanagiguchi, S. Yamada, Y. Hayashi, Biomed. Res. Int. **2014**(1), 786892 (2014)

58. T.S. Putri, D. Rianti, P. Rachmadi, A. Yuliati, Mater. Lett. **304**, 130672 (2021)
59. N.B. Milosavljevic, N.Z. Milasinovic, I.G. Popovic, J.M. Filipovic, Polym. Int. **6**(3), 443–452 (2011)
60. P.M.C. Torres, N. Ribeiro, C.M.M. Nunes, A.F.M. Rodrigues, A. Sousa, S.M. Olhero, Biomater Adv. **134**, 112690 (2022)
61. J.C. Ashworth, S.M. Best, R.E. Cameron, Mater. Technol. **29**, 281 (2014)
62. F. Mukasheva, L. Adilova, A. Dyussenbinov, B. Yernaimanova, M. Abilev, D. Akilbekova, . Front. Bioeng. Biotechnol. **12**, 1444986 (2024)
63. B. Yang, X. Li, S. Shi, X. Kong, G. Guo, M. Huang, F. Luo, Y. Wei, X. Zhao, Z. Qian, Carbohydr. Polym. **80**(3), 860–865 (2010)
64. M.S.U. Rahman, J. Wu, H. Chen, C. Sun, Y. Liu, S. Xu, Adv. Phys.: X. **8**(1), 2153624 (2022)
65. M. Cheng, J. Janzekovic, R. Finze, M. Mohseni, S. Saifzadeh, F.M. Savi, O. Ung, M. Wagels, D.W. Hutmacher, Bioengineering **11**, 593 (2024)
66. G. Rijal, W. Li, Sci. Adv. **3**, e1700764 (2017)
67. J.A. Sowjanya, J. Singh, T. Mohita, S. Sarvanan, A. Moorthi, N. Srinivasan, N. Selvamurugan, Colloids Surf. B Biointerfaces **109**, 294 (2013)
68. D. Rianti, G. Fanny, R.V. Nathania, A.E. Purnamasari, R.R. Putri, H. Soekartono, Soebagio, A. Yuliati, and A. Syahrom 2022 Int. J. Integr. Eng. 14(2): 13
69. S.L. Levengood, M. Zhang, J. Mater. Chem. B Mater. Biol. Med. **2**(21), 3161–3184 (2014)
70. Y.D. Nokoorani, A. Shamloo, M. Bahadoran, H. Moravvej, Sci. Rep. **11**, 16164 (2021)
71. K. Zhou, F.A. Azaman, Z. Cao, M.B. Fournet, D.M. Devine, Macromol. **3**, 326–342 (2023)
72. Y. Privar, A. Skatova, M. Maiorova, A. Golikov, A. Boroda, S. Bratskaya, Gels **10**, 483 (2024)
73. P. Domalik-Pyzik, J. Chlopek, and K. Pielichowska, Springer, Cham, **56**, 1665–1693 (2019)
74. A. Sienkiewicz, P. Krasucka, B. Charmas, W. Stefaniak, J. Goworek, J. Therm. Anal. Calorim. **130**, 85 (2017)
75. P. Chhabra, P. Tyagi, A. Bhatnagar, G. Mittal, A. Kumar, J Pharm Bioallied Sci. **8**(4), 300–308 (2017)
76. S. Pramanik, A. Aggarwal, A. Kadi, M. Alhomrani, A.S. Alamri, W.F. Alsanie, K. Koul, A. Deepak, S. Bellucci, RSC Adv. **14**, 19219–19256 (2024)
77. M.R.D. Cunha, F.L.M. Maia, A. Iatecola, L.C. Massimino, A.M.d.G. Plepis, V.d.C.A. Martins, D.N.D. Rocha, E.D. Mariano, M.C. Hirata, J.R.M. Ferreira, M.L. Teixeira, D.V. Buchaim, R.L. Buchaim, B.E.G.D. Oliveira, and A.A. Pelegrine 2023 J. Funct. Biomater 14(7): 357
78. G. Morello, G.D. Laco, G. Gigli, A. Polini, F. Gervaso, Gels **9**(2), 132 (2023)
79. P. Coimbra, P. Ferreira, H.C. de Sousa, P. Batista, M.A. Rodrigues, I.J. Correia, M.H. Gil, Int. J. Biol. Macromol. **48**, 112–118 (2011)
80. G.-F. Ma, A. Ali, N. Verzijl, R. Hanemaaijer, J. TeKoppele, Y.T. Konttinen, J. Salo, Arthritis Rheum. **54**(9), 2928–2933 (2006)
81. A. Setiawati, D.S. Candrasari, S.D.E. Setyajati, V.K. Prasetyo, D. Setyaningsih, Y.S. Hartini, Asian Pac. J. Trop. Biomed. **12**, 279 (2022)
82. A. Setiawati, D. Jang, D. Cho, S. Cho, H. Jeong, S. Park, J. Gwak, S.R. Ryu, W.H. Jung, B.G. Ju, K.H. Jung, O.S. Kwon, K. Shin, Adv. Healthc. Mater. **10**, 1 (2021)
83. M.C. Ratri, A.I. Brilian, A. Setiawati, H.T. Nguyen, V. Soum, K. Shin, Adv Nanobiomed Res. **1**(5), 2000088 (2021)
84. X. Li, Y. Jin, J. Xue, Int. J. Gen. Med. **17**, 1773 (2024)
85. C.E. Barcus, E.C. Holt, P.J. Keely, K.W. Eliceiri, L.A. Schuler, PLoS ONE **10**(1), e0116891 (2015)
86. J. Jokinen, E. Dadu, P. Nykvist, J. Käpylä, D.J. White, J. Ivaska, P. Vehviläinen, H. Reunanen, H. Larjava, L. Häkkinen, J. Heino, J. Biol. Chem. **279**(30), 31956 (2004)
87. V. Gkretsi, T. Stylianopuolos, Front. Oncol. **8**, 1 (2018)
88. B. Yue, J. Glaucoma **23**, S20 (2014)
89. J. Yao, K. Deng, J. Huang, R. Zeng, J. Zuo, Cancer Front. Pharmacol. **11**, 1 (2020)
90. A.D. Leeper, J. Farrell, L.J. Williams, J.S. Thomas, J. Michael Dixon, S.E. Wedden, D.J. Harrison, and E. Katz 2012 Biomaterials 33(3): 907
91. C.J. Lovitt, T.B. Shelper, V.M. Avery, BMC Cancer **18**, 1 (2018)
92. M.C. Leiva, E. Garre, A. Gustafsson, A. Svanström, Y. Bogestål, J. Håkansson, A. Ståhlberg, G. Landberg, J. Cell. Physiol. **236**, 4709 (2021)
93. J. Dittmer, B. Leyh, Semin. Cancer Biol. **31**, 3 (2015)
94. M.B. Meads, R.A. Gatenby, W.S. Dalton, Nat. Rev. Cancer **9**, 665 (2009)
95. D.S. Lee, J.I. Kang, B.H. Hwang, K.M. Park, Macromol. Res. **27**, 205–2011 (2019)